Solar Energy Materials and Solar Cells 201 (2019) 110053

Contents lists available at ScienceDirect

Solar Energy Materials and Solar Cells

journal homepage: www.elsevier.com/locate/solmat

Evidence for plasmonic hot electron injection induced superior visible light photocatalysis by g-C_3N_4 nanosheets decorated with Ag–TiO_2(B) and Au–TiO_2(B) nanorods

Kamal Kumar Paul[a], P.K. Giri[a], H. Sugimoto[b], Minoru Fujii[b], Biswajit Choudhury[c,*]

[a] Department of Physics, Indian Institute of Technology Guwahati, Guwahati, 781039, India
[b] Department of Electrical and Electronic Engineering, Graduate School of Engineering, Kobe University, Kobe, 657-8501, Japan
[c] Physical Sciences Division, Institute of Advanced Study in Science and Technology, Paschim Boragaon, Vigyan Path, Guwahati, 781035, India

ARTICLE INFO

Keywords:
Hot electrons
Visible light catalysis
Photoluminescence
Plasmonics
Charge transfer
Photoresponse

ABSTRACT

Hot electrons produced by the surface plasmon decay can be efficiently utilized to drive photochemical reactions on a semiconductor surface. Considering this aspect of plasmonics, we have evaluated the visible light photocatalytic performance of Ag–TiO_2(B)–C_3N_4 and Au–TiO_2(B)–C_3N_4 heterostructures in the degradation of rhodamine B (RhB) and phenol. The synergetic effect of plasmonic hot electron injection and interfacial charge transfer in the heterostructures lead to 6–9 fold enhancement in the photodecomposition rate of RhB (phenol) over TiO_2(B) and C_3N_4. Time-resolved photoluminescence study shows fast charge transfer through the integrated network of the heterostructure. The photocurrent is measured at 470 nm, 510 nm and 575 nm, near the plasmonic excitations of Ag and Au as well as under white light illumination (400–800 nm). Plasmonic systems show more than 6-fold enhancement in photocurrent over bare TiO_2(B) under illumination near monochromatic plasmonic excitation. The overall photocurrent resulting from white light illumination is 2-fold stronger than that under plasmonic excitation. The increase is due to the contribution from Ti^{3+} excitation, hot electron injection, and charge transfer from TiO_2(B) to C_3N_4. We propose that Ti^{3+} states in TiO_2(B) provide channels for direct hot electron transfer from metal to semiconductor facilitating charge separation for participation in photocatalysis.

1. Introduction

In 1972, Fujishima and Honda performed the ground-breaking work on H_2 generation by photoelectrochemical water splitting on TiO_2 electrode under UV light irradiation. This remarkable work showed new strategies for efficient utilization of solar energy to generate next-generation green energy sources to fulfill the high energy demand for sustainable development [1]. Wide band gap TiO_2 performs well under UV light, which accounts only ~4% of total solar radiation incident on the earth's surface [1,2]. Harvesting the visible light for chemical energy transformation requires semiconductor with absorption or bandgap in the visible region. Doping with metal and non-metal ions and composite with low band gap semiconductors are widely adopted strategies to develop a semiconductor heterostructure (HS) with effectively narrow band gap [3–8]. Even though doping triggers optical absorption in the visible region, it compromises the photocatalytic efficiency of the system by acting as carrier recombination sites [4]. A TiO_2 based semiconductor HS with low band gap sulfide semiconductors tends to have better interfacial charge separation. The composite, however, suffers from sulfur dissolution in the aqueous medium during photochemical reactions [7]. Very recently, plasmonic photocatalysis has emerged as the newest addition to the field of heterogeneous photocatalysis, whereby noble metal nanoparticles (NPs) displaying size and shape tunable surface plasmon resonance (SPR) band in the visible and near-infrared (NIR) region can boost up the photocatalytic activity of the semiconductor systems [9–11]. Plasmon-driven photochemistry can overcome the photocatalytic limitations encountered with wide-band gap semiconductors, such as weak response to visible-NIR light, the high recombination rate of photogenerated carriers, etc. [12]. Enhancement of the photocatalytic activity in metal oxides decorated with plasmonic nanoparticles occurs via different processes [10,12,13]. These include (i) hot electron generation and injection into semiconductor either by an indirect or direct way. In an indirect process, the hot electron is transferred to TiO_2

* Corresponding author.
E-mail addresses: biswajitchoudhury@iasst.gov.in, biswa.tezu@gmail.com (B. Choudhury).

https://doi.org/10.1016/j.solmat.2019.110053
Received 18 December 2018; Received in revised form 1 July 2019; Accepted 11 July 2019

surpassing the Schottky barrier at the metal-semiconductor interface, whereas in the direct process the hot electrons are directly excited into the semiconductor, (ii) localized electromagnetic field enhancement in the near-surface region of the semiconductor followed by electron-hole generation, (iii) plasmon resonance energy transfer from metal to semiconductor through dipole-dipole interaction.

In this work, we report on the superior photocatalytic performance in the degradation of RhB and phenol by a three-component plasmonic photocatalyst of Ag–TiO_2(B)–C_3N_4 and Au–TiO_2(B)–C_3N_4 under the illumination of visible light. There are very few reports on the visible light photocatalytic activity of Ag–TiO_2(B)–C_3N_4 and Au–TiO_2(B)–C_3N_4 ternary hybrids for H_2 production, CO_2 reduction, and water purification [14–17]. The mechanism for the superior photocatalytic activity is often attributed to the SPR of plasmonic metal nanoparticles, plasmon excitation in the nearest semiconductors and interfacial separation and transfer of photogenerated electrons and holes. These studies have considered anatase or rutile forms of TiO_2 for photocatalysis. Herein, we have considered mesoporous monoclinic porous TiO_2(B) nanorods (NRs) as the host material to decorate the plasmonic metal NPs (Au, Ag). TiO_2(B) NRs have layered structures with lower packing density and open channels. This uniqueness makes TiO_2(B) a suitable candidate over its other polymorphs, anatase, and rutile in binding the plasmonic NPs over its surface [18,19]. In this article, we have discussed the synergetic effect of defect-mediated hot electron injection and interfacial charge separation in the photocatalytic efficiency. The ternary plasmonic photocatalysts display active utilization of the entire solar energy spectrum via the activation of plasmonic absorption. Plasmonic activation results in hot electron generation and their subsequent transfer to the nearest semiconductor (TiO_2) via the intermediate trap states present in the semiconductors. The result of photocatalysis is supported by photocurrent response study, which demonstrates the pivotal role of hot electron injection and interfacial charge transfer mediated enhancement of photocatalysis in the system.

2. Experimental

2.1. Synthesis

The details of the experimental procedure for the synthesis of TiO_2(B), g-C_3N_4 and plasmonic HSs are given in section S1, electronic supporting information (ESI). Typically, TiO_2(B) NRs was prepared by a hydrothermal method in a 100 mL autoclave maintained at 180 °C for 16 h [6]. The components in the autoclave were TiO_2 powder, aqueous ethylene glycol, and NaOH. The product obtained after hydrothermal treatment was washed with 0.1 N HCl and the final product was calcined at 500 °C for 5 h in the air to obtain monoclinic TiO_2(B) phase. g-C_3N_4 (CN) was prepared following the procedure mentioned in our earlier report [20]. Colloidal Au and Ag NPs were prepared by a citrate reduction method following earlier reports [21,22]. Au and Ag NPs decorated over TiO_2(B) NRs was prepared by an in-situ deposition method. TiO_2(B) NRs were mixed with 0.5 mM silver nitrate/gold chloride solution, and the solution was heated to boiling. To this solution, 30 mM trisodium citrate dehydrate solution was added dropwise under stirring condition. The stirring was stopped following color change to light purple and greenish yellow in case of Au and Ag NPs, respectively. The product was washed with deionized water and dried at 60 °C. To decorate Ag–TiO_2(B) or Au–TiO_2(B) NRs over the g-C_3N_4 nanosheets, a certain amount of Ag–TiO_2(B) or Au–TiO_2(B) NRs and g-C_3N_4 was separately dispersed in 2-propanol by ultrasonic mixing for 30 min. The dispersion of Ag–TiO_2(B) and Au–TiO_2(B) NRs was added to the g-C_3N_4 mixture under stirring. The final product was collected after air drying. For simplicity, we will refer the samples Ag–TiO_2(B) as Ag–TiO_2, Au–TiO_2(B) as Au–TiO_2, Ag–TiO_2(B)–C_3N_4 as Ag–TiO_2–CN, and Au–TiO_2(B)–C_3N_4 as Au–TiO_2–CN.

2.2. Characterisations

X-ray diffraction (XRD) of the as-grown catalysts was performed in a Bruker D8 Advance X-ray diffractometer (0.154 nm Cu Kα radiation, 40 kV, 40 mA). Raman scattering measurements were performed in a micro-Raman spectrometer (LabRam HR800, Jobin Yvon) at an excitation wavelength of 488 nm. The surface morphology, structure, and particle size distribution of the as-grown catalysts were studied by a transmission electron microscope (TEM) (JEOL-JEM 2010 operated at 200 kV). Fourier transform infrared (FTIR) spectroscopy measurements were performed in Perkin Elmer, Spectrum BX spectrophotometer. Nitrogen adsorption–desorption isotherms were recorded in a Quantachrome autosorb-iQ MP analyzer at 77 K. Surface area of the catalysts was determined using multipoint Brunauer–Emmett–Teller (BET) method and the average pore size was measured by Barett–Joyner–Halenda (BJH) model. X-ray photoelectron spectroscopy (XPS) measurement was carried out using a PHI X-tool automated photoelectron spectrometer (ULVAC-PHI, Japan) with an Al K_α X-ray beam (1486.6 eV) at a beam current of 20 mA. The shift in the binding energy was corrected using the C 1s spectrum at 284.8 eV as a standard value. UV–Vis diffuse reflectance spectroscopy (DRS) measurements of the samples were recorded using a commercial spectrophotometer (Shimadzu 2600). The room temperature (RT) steady state PL spectra of the samples were recorded with the help of a spectrometer (focal length: 15 cm; blaze wavelength: 500 nm; groove density: 150 gmm^{-1}) equipped with a cooled charge-coupled device (Princeton Instruments, PIXIS 100B) detector using a 405 nm diode laser (Coherent, Cube) excitation. Time-resolved photoluminescence (TRPL) spectra were recorded in a picosecond time-resolved fluorescence spectrometer (Edinburg Instruments, FSP920).

2.3. Photocatalytic experiments

Photocatalytic measurements were performed in a photocatalytic reactor equipped with a 250 W visible lamp (wavelength range ~390–800 nm) surrounded by a water-cooled quartz jacket. The experiment was conducted in a 100 mL beaker with 10 mg/L concentration of RhB/phenol and 20 mg of catalyst (section S2, ESI). We performed the photocatalytic experiment under some sacrificial agents to confirm the presence of active radicals and their participation during photocatalysis. In this experiment, ammonium oxalate (AO), tert-butanol (t-BA) and p-benzoquinone (BQ) were used as hole (h^+), hydroxyl radical (•OH) and superoxide radical ($O_2^{\bullet -}$) scavengers, respectively. We also monitored photoluminescence spectra (PL) of terephthalic acid (TA) to quantify the presence of hydroxyl radicals in solution, and UV–vis spectra of nitro-blue tetrazolium chloride (NBT) to detect the superoxide radicals' present in solution (section S2, ESI).

2.4. Photocurrent response study

Pristine TiO_2, CN and their HSs with Ag and Au NPs were spin coated on a glass substrate to form a homogeneous film of catalysts. Afterward, Al layer of thickness ~100 nm was deposited on the sample with proper masking by a thermal evaporation method (base pressure of $\sim 1 \times 10^{-6}$ mbar) which serves as the electrodes for the photoconductivity measurement. Photoresponse was measured in a microprobe station (ECOPIA EPS − 500) coupled to a source measure unit (Keithley 2400, USA) without and with bias voltage of 10 V. A 250 W Xenon lamp (Newport, 10 USA) was used for the illumination and the excitation wavelength was varied using a monochromator (Oriel Instruments, USA) attached to the lamp. The light intensity on the sample was 3.4 mW/cm^2.

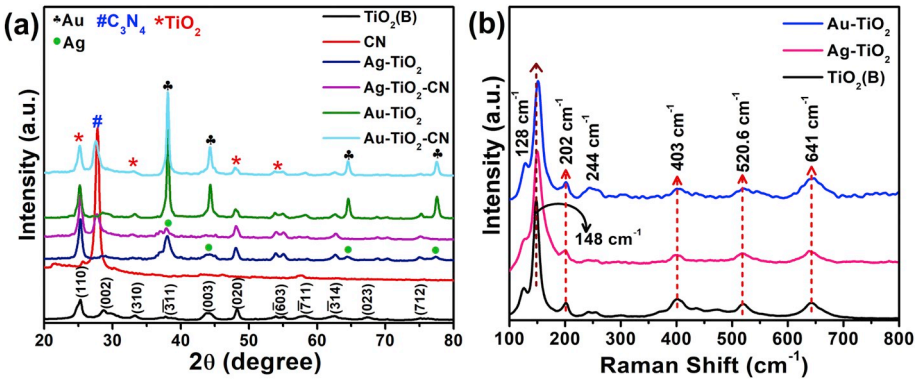

Fig. 1. (a) XRD patterns of pristine TiO_2(B), Ag–TiO_2, Au–TiO_2 and their HS with CN. (b) Raman spectra of Au and Ag NP coated TiO_2(B) NRs.

3. Results and discussion

3.1. Structural studies

XRD patterns of TiO_2, CN, Ag–TiO_2, Au–TiO_2, Ag–TiO_2–CN, and Au–TiO_2–CN are shown in Fig. 1(a). The cubic Au NPs exhibit major diffraction peaks at 38.21, 44.41, 64.61 and 77.61° assigned to (111), (200), (220) and (311) planes, respectively [23]. Ag NPs having diffraction peaks at 38.2, 44.4, 64.5, 77° can be attributed to the planes similar to that of Au due to its identical cubic crystal structure [24]. CN contains a single intense peak at 2θ = 27.8° corresponding to the (002) plane [20]. All the diffraction peaks detected for TiO_2 correspond to the monoclinic phase of TiO_2(B) (JCPDS 74–1940) [6]. Raman scattering of the samples is recorded to identify any local structure change in TiO_2(B) on Au and Ag decoration (Fig. 1(b)). Major scattering peaks at 126, 150.4, 200, 242, 403, 520 and 644 cm^{-1} correspond to TiO_2(B) phase [25,26]. The signal at 145 cm^{-1} matches with that of anatase TiO_2 indicating the fractional growth of anatase along with TiO_2(B) during hydrothermal synthesis [25]. Au–TiO_2(B) and Ag–TiO_2(B) show a marginal blue-shift with a concomitant increase in the full-width at half maximum. This may be due to the compressive stress on the surface atoms of the TiO_2(B) lattice on metal NPs deposition [27]. Because of the strong fluorescence properties of CN, Raman scattering measurement on pristine CN, Ag–TiO_2–CN, and Au–TiO_2–CN HSs under visible light exposure was not successful. Water molecules adsorbed on the catalyst surface can be identified by their characteristic stretching (-OH) and bending (H–O–H) vibration modes in the FTIR spectra at 3431 cm^{-1} and 1592 cm^{-1}, respectively, as shown in Fig. S1 (ESI). The position of –OH is shifted in the plasmonic catalysts. This may be due to the surface modification of TiO_2 on Au and Ag decoration. The Ti–O stretching vibrational modes and the presence of titanate species give rise to the bands at 454.8 cm^{-1}, 805.9 cm^{-1} and 990 cm^{-1}. The stretching and bending vibrations of C–N in the aromatic ring of CN give rise to the bands at 806 cm^{-1} and the multiple absorptions from 1750 to 1150 cm^{-1} [20].

The prepared TiO_2(B) is highly porous as revealed from the TEM image (Fig. S2, ESI). Ag NPs are well dispersed over the TiO_2(B) NRs as revealed from the low and high-resolution TEM images (Fig. 2(a and b)). The low and high-resolution TEM images of Ag–TiO_2–CN are shown in Fig. 2(c) and (d), respectively. Fig. 2(d) shows a good interfacial contact of Ag with TiO_2 distributed over C_3N_4. In comparison to Ag NPs, the size of Au NPs is slightly bigger although well dispersed over TiO_2(B), as shown in Fig. 2(e). Fig. 2(f) shows the Au–TiO_2 over C_3N_4 nanosheet. We have measured the sizes of Ag and Au in the plasmonic hybrid systems. In Ag–TiO_2 and Au–TiO_2, the calculated average sizes of Ag and Au NPs are 7.2 nm and 12.3 nm, respectively (Figs. S3(a–b), ESI). However, Ag and Au NPs grow to 14.9 nm and 16.8 nm in Ag–TiO_2–CN and Au–TiO_2–CN, respectively, as shown in Fig. 2(d and e). The larger size of Ag and Au in the composites is possibly due to pore filling of TiO_2 with CN and subsequent aggregation of Au (or Ag) over TiO_2(B) or CN surface.

We have measured the specific surface area, pore size and pore volume of the samples from the N_2 adsorption-desorption isotherms (see Fig. S4(a), ESI), and the results are included in Table S1. The type of the curves is characteristic of type IV isotherms with a type H_3 hysteresis loop characteristic of the presence of asymmetric, interconnected slit-shaped pores [28]. TiO_2(B) has a specific surface area of 83.2 m^2/g, pore diameter of 32.8 nm and pore volume of 0.65 cc/g. The pore diameter is determined from the BJH pore size distribution as shown in Fig. S4(b) (ESI). The large porosity of TiO_2(B) NRs offers many anchoring sites for the attachment of Ag and Au NPs. As Table S1 shows, the porosity and the total surface area diminishes once TiO_2(B) is decorated with Ag and Au NPs and CN. The possible reason could be the filling up of pores, pore blocking and shrinking with deposited metal NPs and CN [29].

Fig. 3(a–f) shows the core-level XPS spectra of different elements present in Ag–TiO_2–CN and Au–TiO_2–CN. The core level Ti 2p XPS spectrum of each HS can be identified with two doublets located at ~458.7 eV (Ti2$p_{3/2}$) and ~464.3 eV (Ti2$p_{1/2}$), respectively. This is depicted in Figs. S5(a) and 5(d) (ESI) for Ag–TiO_2 and Au–TiO_2, and Fig. 3(a,d) for Ag–TiO_2–CN and Au–TiO_2–CN, respectively. The splitting of 5.6 eV is an indication of normal Ti^{4+} state in TiO_2(B) [4]. In addition to the major doublets, each Ti 2p XPS spectrum of the HS samples contains two shoulder peaks at ~457 eV (Ti $2p_{3/2}$) and ~461.3 eV (Ti$2p_{1/2}$). These minor shoulder peaks are attributable to Ti^{3+} states [30]. The percentage of Ti^{3+} is calculated from the corresponding relative area percentage by Gaussian fittings with Shirley baseline. The calculated amount of Ti^{3+} is 6.9% in TiO_2, 10.3% in Ag–TiO_2, 8.1% in Au–TiO_2, 12.0% in Ag–TiO_2–CN, and 8.9% in Au–TiO_2–CN. The core-level O 1s XPS spectra corresponding to Ag–TiO_2, Au–TiO_2 (Figs. S5(b) and 5(e), ESI) and Ag–TiO_2–CN and Au–TiO_2–CN (Fig. 3(b) and (e)) are deconvoluted with four peaks. The peaks at 530.0 eV, 531.2 eV, 532.7 eV, and 534.8 eV can be assigned to lattice oxygen ($TiO_{lattice}$), oxygen vacancy (Ov)-Ti^{3+} surface states, –OH group attached to the surface of TiO_2, and possibly C–O bonding with surface CN or TiO_2, respectively [30–32]. The Ag 3d XPS spectrum of Ag–TiO_2 are identified with two characteristic doublets at 368.0 eV ($3d_{5/2}$) and 374.0 eV ($3d_{3/2}$) with an energy separation of 6 eV corresponding to metallic Ag (0), see Fig. S5(c) in ESI [33]. Similar doublets are seen in the Ag 3d XPS spectrum of Ag–TiO_2–CN, as shown in Fig. 3(c). The peak position of deposited Ag NPs got shifted to lower binding energy by an amount of 0.2 eV in comparison to that of bulk Ag (368.3 eV and 374.3 eV) [34]. The XPS spectrum of Au 4f has been identified with doublets at 83.0 eV ($4f_{7/2}$) and 86.6 eV ($4f_{5/2}$) characteristic of metallic Au(0), as shown in Fig. S5(f) (ESI) for Au–TiO_2 and Fig. 3(f) for Au–TiO_2–CN. In comparison to the peak positions reported in unsupported Au (84.0 eV and 87.7 eV) [34], we encountered a negative shift of −1.0 eV. The negative shift results from the strong metal-support interaction leading

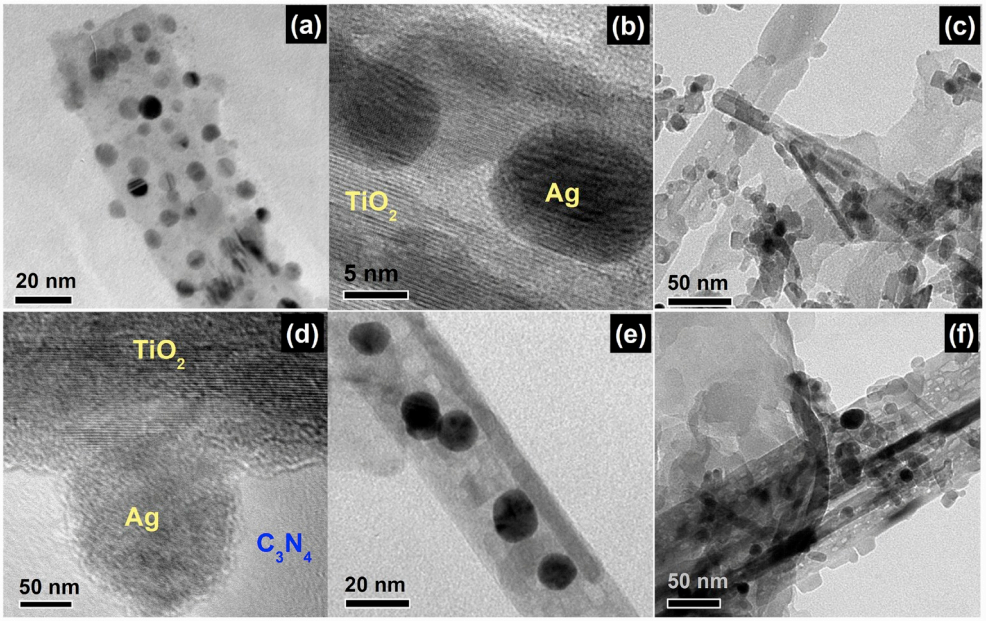

Fig. 2. (a) TEM image of Ag–TiO_2 HS, (b) magnified view of Ag NP over TiO_2 NR. (c) TEM image of Ag–TiO_2–CN and (d) enlarged view of Ag NP and TiO_2 NR over CN nanosheet. (e) TEM image of Au–TiO_2. (f) TEM image Au–TiO_2–CN HS.

to an efficient electron transfer from TiO_2 to the metal [23]. The electron transfer occurs via the Au(or Ag)–Ti^{3+} bonding and imparts a negative charging over the metal nanoparticles. Studies have shown that metal interacts strongly with the Ti^{3+}/oxygen vacancy sites on TiO_2 surface [35,36]. We could not derive any relevant information from the C 1s and N 1s XPS spectra of Ag–TiO_2–CN and Au–TiO_2–CN (Figs. S6(a–d)). The detail discussion of the spectrum, therefore, has been provided as ESI.

3.2. Optical studies

The SPR properties of Au and Ag NPs show a strong dependency on the dielectric constant of the surrounding medium. It can be manifested from the SPR band of colloidal Au solutions at ~527 nm (Fig. S7, ESI), and that of Au–TiO_2 at 543 nm (Fig. 4). We, however, have not noticed any change in the SPR band of Au–TiO_2–CN in comparison to that of Au–TiO_2. The SPR band of colloidal Ag NPs at 468 nm is shifted to 514 nm and 480 nm in Ag–TiO_2 and Ag–TiO_2–CN, respectively. The shift in the absorption is because of a change in the dielectric constant of the environment surrounding gold and silver nanoparticles. The reported values of dielectric constants (ε_m) for water is 1.77, ε_m ~ 4.8 for TiO_2, and ε_m ~ 7.2 for CN. A change in the dielectric constant can have a substantial influence on the strength of the interfacial coupling between plasmon and the media leading to either blue or red-shift in the plasmon peak [37–40].

We can understand the charge carrier dynamics in the plasmonic

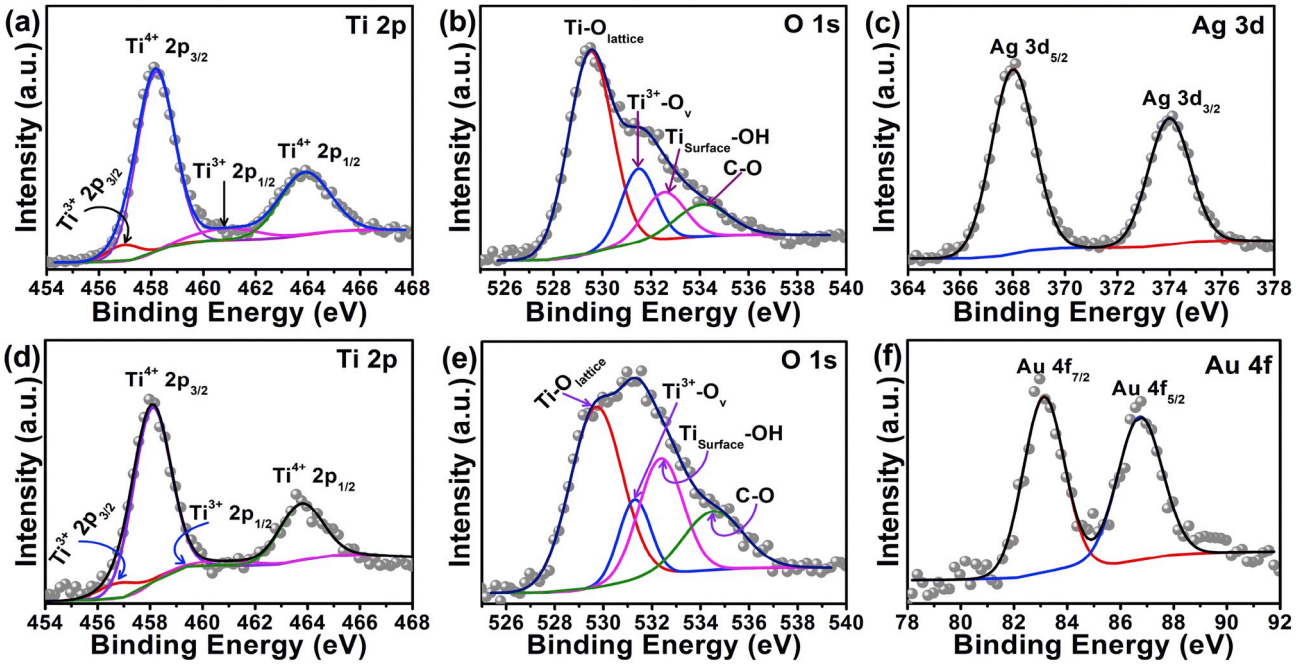

Fig. 3. XPS spectra of Ag–TiO_2–CN and Au–TiO_2–CN with (a,d) Ti 2p, (b,e) O 1s, (c) Ag 3d and (f) Au 4f, respectively.

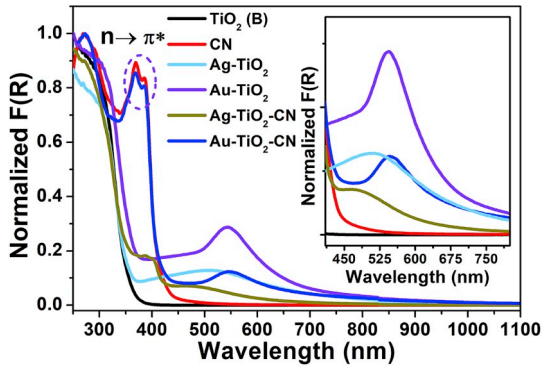

Fig. 4. Kubelka – Munk plot, F(R), derived from the diffuse reflectance spectra of different samples. Inset shows the magnified view in the range 350–780 nm.

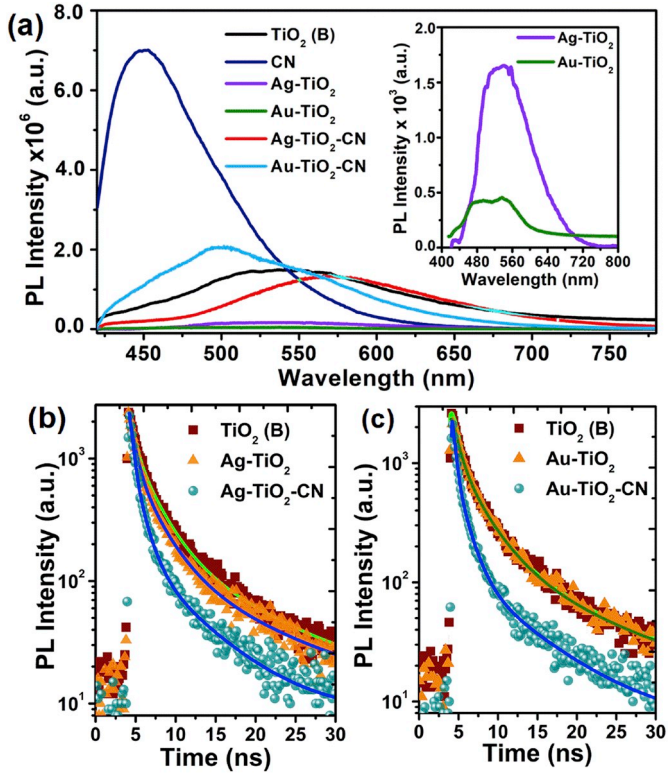

Fig. 5. (a) Steady-state PL spectra of pristine TiO_2, CN and their plasmonic systems. Inset shows the magnified view of PL spectra for Ag–TiO_2 and Au–TiO_2. TRPL spectra of (b) TiO_2 and CN composites with Ag NPs, and (c) TiO_2 and CN composites with Au NPs.

HSs with the aid of steady-state and time-resolved PL spectroscopy. Fig. 5(a) shows the PL spectra of the samples under a photoexcitation wavelength of 405 nm. Pristine TiO_2 shows an emission at 540 nm associated with oxygen defect centers [30]. Surface defects in TiO_2 passivate on Au and Ag loading due to the possible electron transfer from the conduction band or shallow trap states of TiO_2 to Au or Ag [41]. Thus, a reduced PL intensity of the 540 nm emission can be seen in Ag–TiO_2 and Au–TiO_2, as shown in the inset of Fig. 5(a). CN shows a strong excitonic blue emission [42]. However, when Ag–TiO_2 and Au–TiO_2 are loaded with CN, the HSs display a reduced PL intensity. Besides, the emission at 520 nm in Ag–TiO_2 is red-shifted to 580 nm in Ag–TiO_2–CN. The emission at 520 nm in Au–TiO_2 is blue-shifted to 500 nm in Ag–TiO_2–CN. The plausible reasons for the suppression of excitonic emission in CN are exciton-plasmon interaction, excitons dissociation with subsequent charge transfer from Au–TiO_2 to CN nanosheets [43,44]. Blue or red spectral shift might also be the outcome of

Table 1
Summary of time resolved PL results: average carrier life time (τ_{av}), charge transfer time (τ_{CT}) and charge transfer efficiency (η).

Sample	Lifetime (ns)			τ_{av} (ns)	τ_{CT} (ns)	η
	τ_1 (a_1)	τ_2 (a_2)	τ_3 (a_3)			
TiO_2	0.9 (0.23)	3.0 (0.46)	11.2 (0.31)	8.6	–	–
Ag–TiO_2	0.6 (0.17)	2.5 (0.48)	10.0 (0.35)	7.8	84.0	9.3%
Ag–Ti–CN	0.4 (0.28)	1.3 (0.4)	6.4 (0.32)	5.2	13.1	39.5%
Au–TiO_2	0.7 (0.32)	2.7 (0.41)	10.8 (0.27)	8.1	140.0	5.7%
Au–TiO_2–CN	0.3 (0.28)	1.4 (0.41)	7.5 (0.31)	6.1	22.2	28%

exciton-plasmon interaction, and near-field plasmon coupling of Au/Ag NPs with the defect or excitonic states in Au–TiO_2–CN or Ag–TiO_2–CN. To support our assumptions of an interfacial charge transfer process, we have performed TRPL measurement of the samples. Fig. 5(b and c) shows the TRPL spectra of Ag and Au decorated plasmonic HSs. The TRPL results are recorded at an excitation of 405 nm corresponding to the maximum emission in the respective samples. The decay parameters are obtained from the individual spectrum by tri-exponential fitting, and the resultant data are shown in Table 1. In Table 1, the component τ_1 for pure TiO_2(B) can be associated with self-trapped excitons, and the long components (τ_2, τ_3) originate from bound excitons related with Ti^{3+} and oxygen vacancies [45]. The three components become shorter after decorating TiO_2 with Au, Ag, and CN. The shortening of carrier lifetime is possibly due to a charge transfer interaction between Ti^{3+} and Ag (or Au) at the Ag–TiO_2 and Au–TiO_2 interface. There is a further shortening of carrier lifetimes in Ag–TiO_2–CN and Au–TiO_2–CN. We have measured the average lifetime for each sample and determined the charge-transfer time following the relation [46]:, $\tau_{CT} = \frac{\tau_{Semi}\tau_{Hybrid}}{\tau_{Semi} - \tau_{Hybrid}}$. Moreover, the efficiency of the charge transfer is measured as $\eta\% = \frac{\tau_{Hybrid}}{\tau_{CT}}$. The corresponding values of τ_{CT} and η are included in Table 1. It is noticed that τ_{CT} decreases from 84 ns in Ag–TiO_2 to 13.1 ns in Ag–TiO_2–CN with an associated increase in η from 9.3% to 39.5%. Similarly, a reduced τ_{CT} from 140 ns to 22.2 ns is observed when Au–TiO_2 is hybridized with CN with η enhancement from 5.7% to 28%.

3.3. Photocatalytic study

Fig. 6(a) shows the temporal change in the absorption intensity of RhB under visible light irradiation in the presence of Ag–TiO_2–CN. Blank RhB shows a maximum absorption peak at 550 nm. This peak falls in intensity as light irradiation continues and at 100 min this peak completely disappears. Fig. 6(b) shows the efficiency of different catalysts for the degradation of RhB in an aqueous solution. Measurement of the photocatalytic activity under dark reveals that Ag–TiO_2–CN is quite effective in removing 20% of RhB. On exposure to light, about 90% of RhB degradation has been achieved for an irradiation time of 60 min. The determination of first-order rate kinetics reveals that RhB degradation is very fast in the presence of Ag–TiO_2–CN (Fig. 6(c)). The results of RhB degradation and rate constant (k, min^{-1}) are summarized in the form of a histogram in Fig. 6(d). It is observed that the pristine TiO_2(B) NR shows ~44% degradation efficiency with a first order rate constant of 6.5×10^{-3} min^{-1}. On decorating the NRs with Ag NPs, the % degradation and rate constant are increased to ~92% and 2.0×10^{-2} min^{-1}, respectively. Similarly, Au–TiO_2 shows 84% degradation of RhB with a first-order rate constant of 1.7×10^{-2} min^{-1}. Ag–TiO_2–CN achieves ~98% RhB degradation having a rate constant of 4.1×10^{-2} min^{-1}. In the case of Au–TiO_2–CN, the degradation is ~95% with a rate constant of 2.6×10^{-2} min^{-1}. Thus, the three component plasmonic photocatalysts Ag–TiO_2–CN and Au–TiO_2–CN exhibit much improved photocatalytic efficiency as compared to the binary plasmonic systems of Ag–TiO_2 and Au–TiO_2.

Next, we have checked the reusability of Ag–TiO_2–CN as a photocatalyst. The degradation is monitored after each run, and after 6th

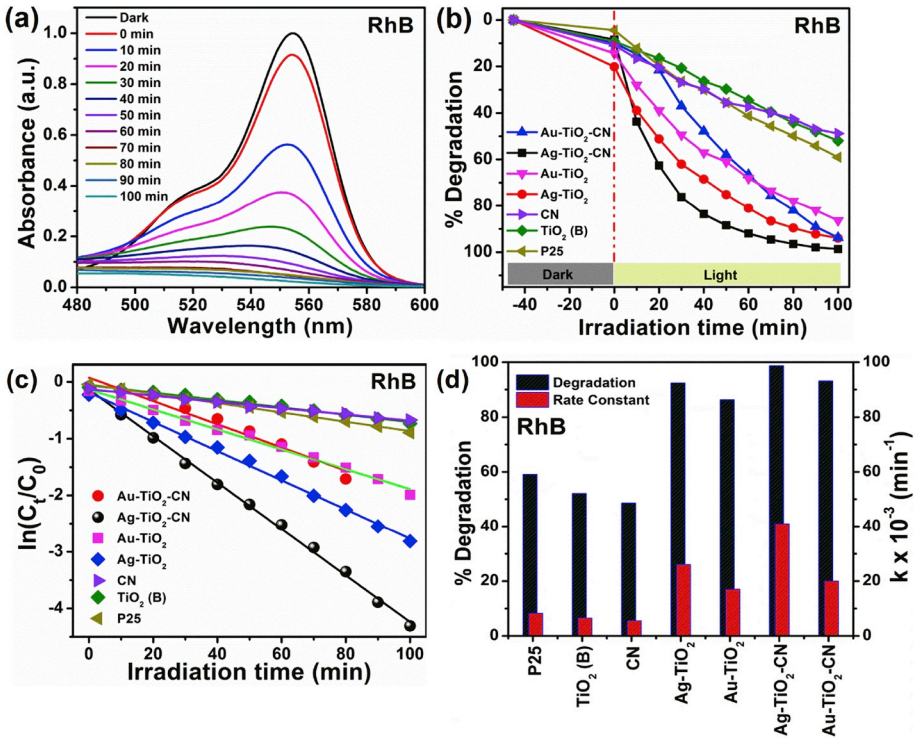

Fig. 6. (a) Photodegradation of RhB in the presence of Ag–TiO_2–CN under the illumination of visible light. (b) Comparison of the photocatalytic activity of different catalysts in the degradation of RhB under dark and light condition. (c) First order rate constant from the linear fitting of $\ln(C_t/C_0)$ vs. irradiation time (t) plot. (d) A comparison of the reaction rate constant and % degradation for different samples.

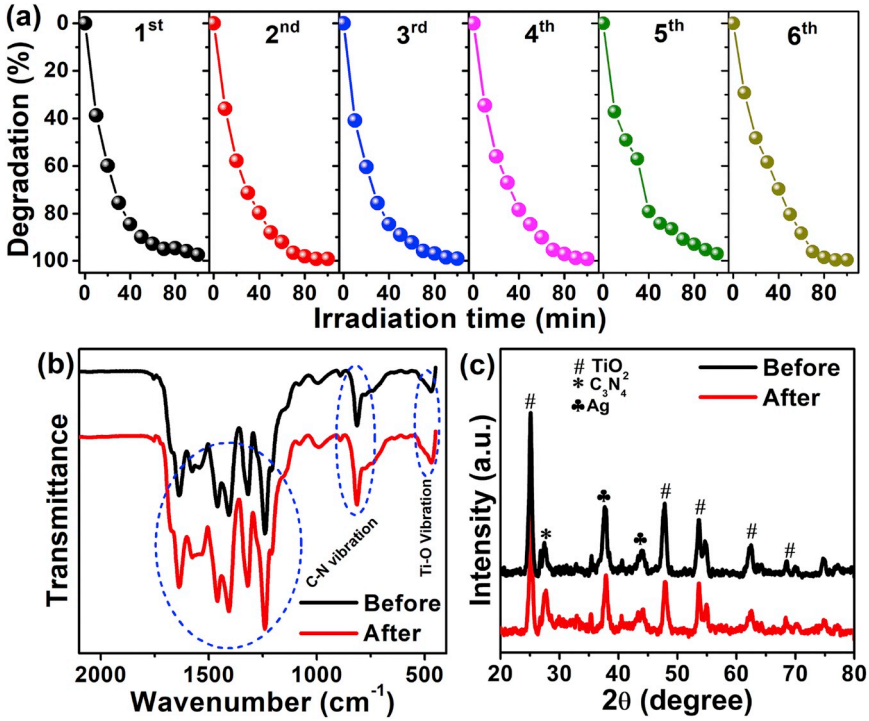

Fig. 7. (a) Cyclic test of Ag–TiO_2–CN up to six consecutive reactions. The measured FTIR (b) and XRD data (c) of Ag–TiO_2–CN before and after the 6th cycle of light irradiation.

cycle we have recorded ~95% photodegradation of RhB (Fig. 7(a)). This implies that the catalyst retains its efficiency in RhB removal at least up to the 6th cycle of reaction. To determine the quality and stability of the catalyst, we have recorded FTIR and XRD patterns of the re-used Ag–TiO_2–CN. The FTIR spectrum of Ag–TiO_2–CN before and after the photocatalysis is shown in Fig. 7(b). No notable change is detected in the vibrational modes of the catalyst after the 6th cycle of photodegradation. Similarly, the crystallinity of Ag–TiO_2–CN is preserved after the 6th cyclic run, as shown in Fig. 7(c). These results demonstrate the superior stability of the photocatalyst under the irradiation of full visible light spectrum. A few radical scavenging tests are undertaken to find out the active radicals participating in photocatalysis. The result of the test is shown in Fig. 8(a). AO, t-BA, and p-BQ are the active scavengers for h^+, •OH and $O_2^{\bullet -}$ radicals, respectively. As shown in the bar diagram of Fig. 8(b), degradation of RhB decreases from ~98% (without any scavenger) to ~60% and ~50% on addition

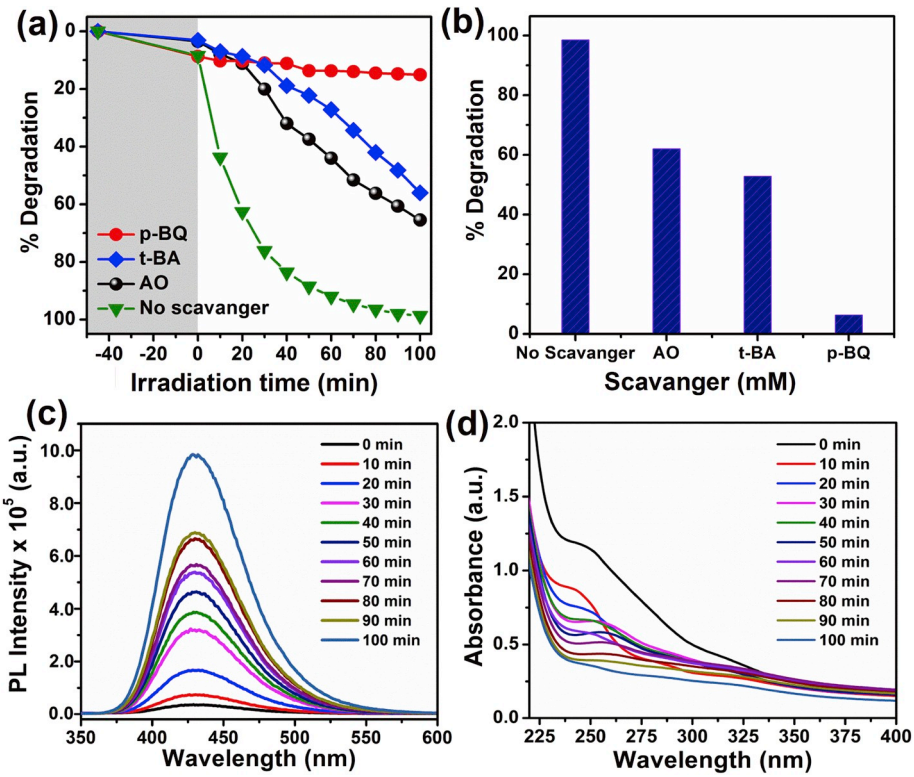

Fig. 8. (a) Degradation of RhB in the presence of various radical scavengers, (b) a comparison of the photocatalytic efficiency of Ag–TiO_2–CN with and without any radical scavengers. (c) Fluorescence spectra of TA and (d) absorbance spectra of NBT with Ag–TiO_2–CN suspension at different irradiation times.

of h^+ scavenger (AO) and •OH scavenger (t-BA), respectively [20]. Interestingly, only ~10% of RhB degradation is achieved when p-BQ is added to the solution containing RhB and Ag–TiO_2–CN. The scavenging test reveals that the RhB degradation is suppressed predominantly in the absence of superoxide radicals ($O_2^{\bullet -}$). Furthermore, terephthalic acid (TA) and NBT test can further support the result of scavenging tests [23]. In the presence of OH, TA is converted to 2-hydroxy terephthalic acid in the aqueous solution and shows strong fluorescence at 445 nm, as shown in Fig. 8(c). The intensity of the fluorescence measures the numbers of OH radicals available in the solution. In solution, OH radicals can also generate from O_2 by following the step: $O_2 + 3e^- + 2H^+ \rightarrow$ •OH + –OH. Thus, the presence of superoxide radicals in solution may also form OH radicals indirectly. We performed the NBT test to identify the presence of $O_2^{2\bullet -}$ radicals, as shown in Fig. 8(d). The absorption peak of NBT at 255 nm shows a monotonous decrease in intensity with the increase in irradiation time. As irradiation time progresses, a larger concentration of superoxide ions interact with NBT and transforms it into blue formazon with a reduction in absorption peak intensity. The results of TA and NBT test are in agreement with the results obtained from radical scavenging test, confirming the major role of O^{2-} radicals in driving the enhanced photodegradation.

The parameters that govern the efficiency of a visible light photocatalyst are its surface area, intense absorption in the visible region, and available free charge carriers. The influence of the surface area on the kinetics of the photocatalytic reaction can be determined by comparing the kinetic rate constant per unit surface area (k/S_{BET}) for different samples [47]. The results of k/S_{BET} for RhB degradation are displayed in Table 2. Although the binary (Ag–TiO_2, Au–TiO_2) and ternary (Ag–TiO_2–CN, Au–TiO_2–CN) plasmonic composites possess lower surface area than pristine TiO_2, the k/S_{BET} is higher in these samples. These results indicate that surface area does not have a prominent role in the overall enhancement of the photocatalytic activity of the hybrid structure. Based on this observation, we believe that SPR absorption,

Table 2
Summary of results for k/S_{BET} from the BET surface area and the 1st order rate kinetics of photodegradation of each catalyst.

Sample	BET surface area (m^2/g)	Rate constant (k) × 10^{-3} (min^{-1})		k/S_{BET} ($min^{-1}m^{-2}g$)	
		RhB	Phenol	RhB	Phenol
TiO_2	83.2	6.5	7.7	7.8×10^{-5}	9.2×10^{-5}
CN	69.5	5.5	5.1	7.9×10^{-5}	7.3×10^{-5}
Ag–TiO_2	26.4	20	23	7.5×10^{-4}	8.7×10^{-4}
Au–TiO_2	28.6	17	19	5.9×10^{-4}	6.4×10^{-4}
Ag–TiO_2–CN	30.0	41	48	1.3×10^{-3}	1.5×10^{-3}
Au–TiO_2–CN	34.0	26	32	7.6×10^{-4}	9.4×10^{-4}

interfacial charge carrier separation, and charge transfer are the main driving forces for the enhanced photocatalytic activity in the hybrid plasmonic systems.

We have tested the photocatalytic activity of the samples with another toxic organic compound, phenol. Since RhB absorbs in the visible light, the photosensitisation induced self-degradation is often considered the reason for the high rate of degradation of RhB with no role of catalyst in this process. However, since phenol absorbs in the UV region, there is no photosensitisation effect on phenol due to visible light, and any degradation recorded is due to the catalyst effect only. Fig. 9(a) shows the changes in absorption intensity of phenol in the presence of Ag–TiO_2–CN under the visible light illumination. Of note, Ag–TiO_2–CN shows excellent photodegradation of phenol over 40 min of irradiation time. Fig. 9(b) shows a comparison of the efficiency of different catalysts to degrade the phenol, while Fig. 9(c) depicts the 1st order degradation rate kinetics of each catalyst. From Fig. 9(d), it is clear that Ag–TiO_2–CN exhibits the best photocatalytic activity amongst all. It can also be noted that the phenol degrades at a faster rate ($4.8 \times 10^{-2}\,min^{-1}$) than RhB ($4.1 \times 10^{-2}\,min^{-1}$) in the presence of Ag–$TiO_2$–CN. Thus, fairly consistent photocatalytic results are shown by

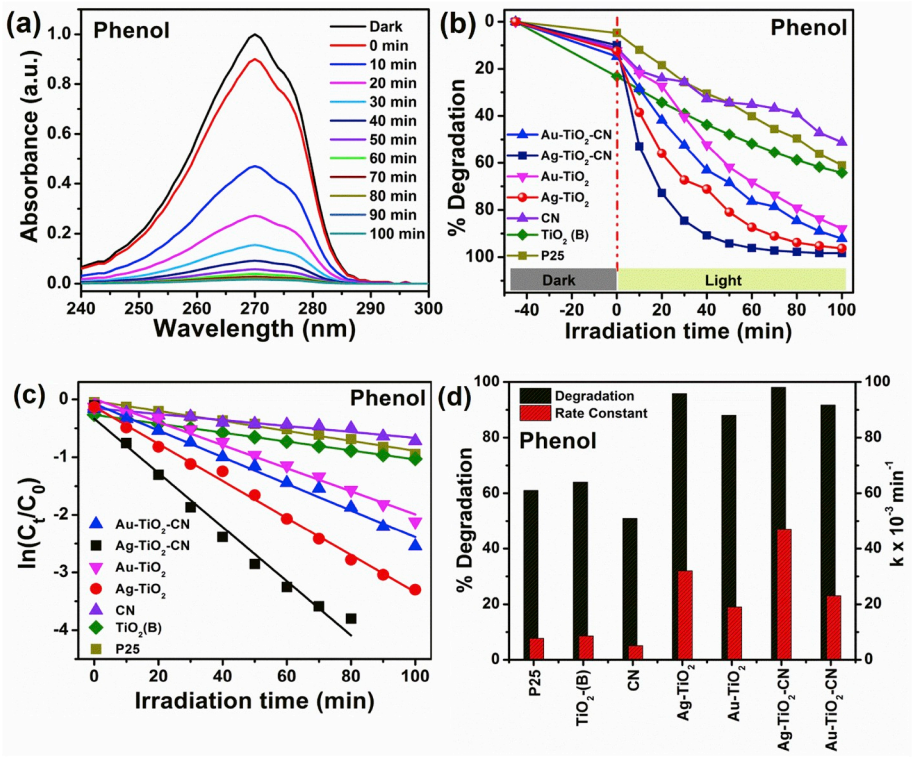

Fig. 9. (a) Photodegradation of phenol in the presence of Ag–TiO_2–CN under the illumination of visible light. (b) Comparison of the photocatalytic activity of different catalysts in the degradation of phenol under dark and light condition. (c) First order rate constant determination from the linear fitting of $\ln(C_t/C_0)$ vs. t plot. (d) A comparison of the maximum rate constant and % degradation achieved by different samples.

Ag–TiO_2–CN in RhB as well as phenol degradation.

3.4. Photocurrent response study

Fig. 10(a) shows a schematic representation of the photoconductivity measurement for the various samples under irradiation at different wavelengths. Fig. 10(b) represents the steady state dark- and photo-current as a function of voltage for the Ag–TiO_2–CN, with the excitation of the whole solar spectrum (> 400 nm). I–V characteristics show more than one order of magnitude enhancement at 5 V after light illumination. Time dependent changes in the photocurrent (I-t) are observed under broadband visible light source using a UV cut-off filter, and under monochromatic irradiation at 510 nm (Fig. 10(c)–(d)). When light is ON, the current sharply rises to its maximum value, and swiftly reduces to zero when light is turned OFF. The ON-OFF light illumination is considered for 3 cycles, and in each cycle, the photocurrent evolution is

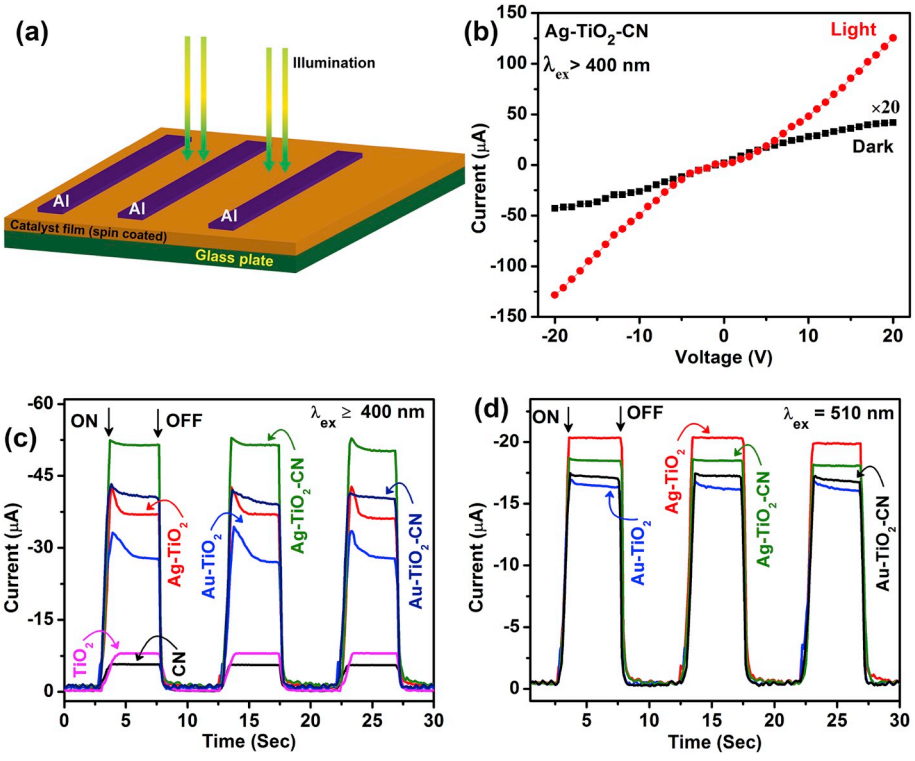

Fig. 10. (a) Schematic of the photoconductivity measurement. (b) Current vs. voltage curve for Ag–TiO_2–CN under dark and visible light illumination (λ ≥ 400 nm). Photocurrent response of binary (Ag–TiO_2, Au–TiO_2) and ternary (Ag–TiO_2–CN, Au–TiO_2–CN) plasmonic photocatalysts with respect to pristine TiO_2 and CN under the illumination of (c) full visible solar spectrum irradiation (λ ≥ 400 nm) and under monochromatic radiation at (d) 510 nm.

stable in the system. We have recorded low photocurrent response in pristine TiO_2 and g-C_3N_4 (Fig. 10(c)). The low photocurrent is possibly due to the large band gap of TiO_2 (~3.2 eV). Even though g-C_3N_4 shows band gap absorption in the visible region, the photocurrent response is minimal, may be due to higher recombination of carriers in the bulk 2D layered nanosheets. The photocurrent enhances by 4-times in Au–TiO_2. The enhancement is nearly ~5.5-times higher in Ag–TiO_2 and Au–TiO_2–CN than that of TiO_2. Highest photocurrent value is recorded for Ag–TiO_2–CN, which is 7-times more than TiO_2 and 9-times higher than CN, as displayed in Fig. 10(c). Next, the photocurrent is measured at 510 nm, which is near to the plasmonic absorption peak of Ag in Ag–TiO_2 (Fig. 10(d)). The measured photocurrent under 510 nm can be arranged as Au–TiO_2 < Au–TiO_2–CN < Ag–TiO_2–CN < Ag–TiO_2. It shows that the plasmon excitation of Ag generates sufficient numbers of hot electrons which contribute to the photocurrent enhancement. The recorded single cycle photocurrent response of Ag–TiO_2–CN under dark and light (λ > 400 nm) is shown in Fig. S8 (ESI). To emulate the condition of photocatalysis experiment, we have measured photoinduced current under white light illumination without any external bias. In the absence of external bias, the device is considered to be operated in photovoltaic mode. Fig. S9 shows the measured photocurrent with incident light switched ON and OFF cyclically. The sample is illuminated under a white light with an intensity of 32.8 mW/cm^2. The plasmonic heterostructure of Ag–TiO_2–CN delivers a stable photocurrent of 1.2 μA, which is 2-fold stronger than Au–TiO_2–CN. The photocurrent measurement, in this case, is the current delivered by the circuit under photovoltaic mode. The built-in potential separates the electrons and holes at the Ag–TiO_2–CN heterojunction, thereby delivering a small photocurrent [48,49].

Next, the photocurrent of each catalyst was measured under 470 nm and 545 nm (Fig. 11(a)-(b)). These wavelengths are close to the plasmonic absorption peak of Ag in Ag–TiO_2–CN (~470 nm), and Au in Au–TiO_2 (~540 nm) and Au–TiO_2–CN (~545 nm). At 470 nm, the photocurrent measurement follows a trend Au–TiO_2 < Au–TiO_2–CN < Ag–TiO_2 < Ag–TiO_2–CN, as shown in Fig. 11(a). The measured photocurrent under 545 nm irradiation can be arranged as Ag–TiO_2 < Ag–TiO_2–CN < Au–TiO_2 < Au–TiO_2–CN (see Fig. 11(b)). Fig. 11(c) shows the maximum photocurrent displayed by various samples under the different wavelength of irradiation. Photoresponse study demonstrates the generation of large photocurrent when the electrode is illuminated at or near their respective plasmonic absorption peaks [50].

The measurement reveals the contribution of plasmonic excitation and interfacial electron transfer as the dominating mechanism for the enhanced photocurrent in Ag–TiO_2–CN under white light illumination. Similarly, photoexcitation near the plasmonic absorption of Ag (470 nm in Ag–TiO_2–CN, 510 nm in Ag–TiO_2), and Au (540 nm in Au–TiO_2, 545 nm in Au–TiO_2–CN) activates plasmonic hot electron injection followed by the interfacial charge transfer from TiO_2 to CN. The photoresponse study supports the fact that photocatalysis in binary and ternary plasmonic systems is regulated by hot electron generation and interfacial charge transfer.

On the basis of the results discussed, the photocatalytic enhancement in Ag–TiO_2, Au–TiO_2, Ag–TiO_2–CN and Au–TiO_2–CN is believed to result from SPR absorption of metal NPs, interfacial charge separation and their transfer through the multiple interfaces of the HS. In order to discuss these phenomena, we have determined the conduction and valence band-edge potential energy of a semiconductor by Mulliken electronegative theory [51–53].

$$E_{CB} = \chi - E^C - 0.5E_g$$

$$E_{VB} = E_{CB} - E_g$$

where E_{CB} is the conduction band-edge potential, E_{VB} is valence-band potential, χ is absolute electronegativity of a semiconductor, which is the geometric mean of the absolute electronegativity of the constituent atoms. E^C is the energy of the free electron on the hydrogen scale,

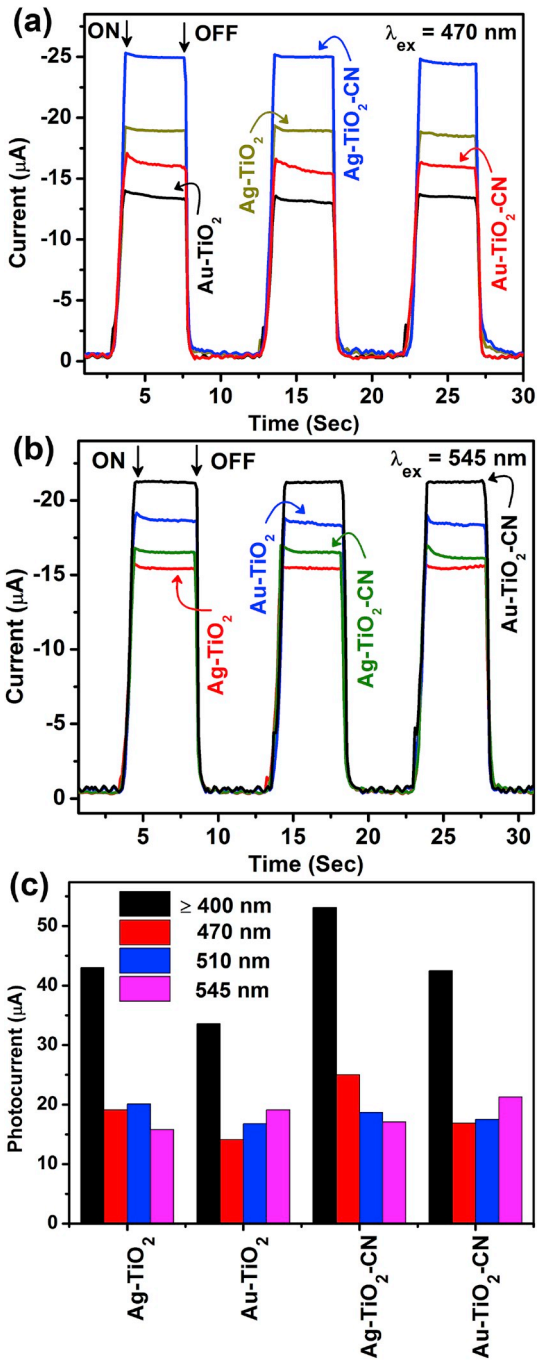

Fig. 11. Measured photocurrent response of the pristine and plasmonic heterostructures under λ_{ex} of (a) 470 nm and (b) 545 nm. (c) Maximum photocurrent recorded for various samples under different illumination.

which is ~4.5 eV, and E_g is the band-gap of the semiconductor. For TiO_2 and CN nanosheets, the χ values are 5.81 eV and 6.9 eV, respectively. The measured values of bandgap for TiO_2 and CN are 3.31 eV and 2.92 eV, respectively. Therefore, E_{CB} and E_{VB} band edge potentials for TiO_2 are estimated to be −0.345 eV and 2.965 eV, respectively. The calculated values of E_{CB} and E_{VB} for CN are determined to be 0.94 eV and 3.86 eV, respectively. The band edge in electrochemical scale and absolute vacuum scale (AVS) are inter-convertible by following the relation: E_{AVS}(eV) = $-E_{NHE}$ − 4.5 (V) [54]. Therefore, the energies of VB and CB edges for TiO_2 are −7.465 eV and −4.155 eV, while these positions for CN are at −8.36 eV and −5.44 eV, respectively. Based on the VB and CB edge positions, we might predict effective interfacial

charge separation in the HSs of CN and TiO_2. The work function of Au NPs and Ag NPs are reported to be at −5.1 eV and −4.7 eV, respectively [55].

3.5. Mechanism for enhanced photocatalysis

3.5.1. Ag–TiO_2 and Au–TiO_2

Based on the results of optical and photoresponse studies, we propose that there are two synergetic plasmonic effects which might be responsible for the enhanced photocatalytic activity in Ag–TiO_2 and Au–TiO_2 HS: (i) Hot electron injection through the metal-semiconductor interface. In this process, the energetic hot electrons transfer to the semiconductor following a direct or indirect electron injection pathways, (ii) localized electromagnetic field enhancement in the vicinity of the metal-semiconductor interface. This radiative coupling between metal-semiconductor requires a field energy equivalent to or higher than the band gap of the semiconductor and depends on the inter-particle gap as well as the distance of metal from semiconductor [12,13]. We will now attempt to explain the plasmonic mediated photocatalytic enhancement based on these two controlling effects.

The plasmonic hot electrons can reach an energy level as high as $\hbar\omega$ above the Fermi level of the metal, where ω is photon frequency. The process of generation and the number density of these hot electrons depend on the shape and size of nanocrystals as well as interparticle separation or the hot spot region [56]. The rate of generation of hot electrons on a nanosphere is expressed by-

$$Rate = \frac{2}{\pi^2}\frac{e^2E_F^2}{\hbar}\frac{(\hbar\omega - \Delta E_b)}{(\hbar\omega)^4}\frac{4\pi}{3}R_0^2\left|\frac{3\varepsilon_0}{2\varepsilon_0 + \varepsilon_{metal}}\right|\cdot E_0^2 \quad (1)$$

Where E_F is the Fermi energy, R_0 is the radius of the nanosphere, $\frac{3\varepsilon_0}{2\varepsilon_0+\varepsilon_{metal}}E_0$ is the electric field inside the nanosphere and E_0 is the external field of light [57]. The high energy hot electrons (E) are distributed in the range $E_F + \Delta E_b < E < E_F + \hbar\omega$ and the low energy hot electrons are distributed in the range $E < E_F + \Delta E_b$, where ΔE_b is the energy of the Schottky barrier [56,57].

As equation (1) shows, the rate is directly proportional to the square of the nanosphere radius (R_o^2). From our results on TEM, we have found that Ag NPs have a size of 7.2 nm, whereas Au NPs have a size of 12.3 nm (see Figs. S3(a and b), ESI). Thus, following equation (1), the density of hot electrons will be higher on the surface of Ag–TiO_2 than on Au–TiO_2. Ag has a longer mean free path for electrons than in Au [57]. This is an added benefit for Ag NPs because the plasmonic energy dissipation due to electron-electron scattering is minimized. Another factor that determines the density of plasmonic hot electrons and its energy amplification is the interparticle gap [58]. TEM shows an average interparticle separation of 3.4 nm in Ag and 4.7 nm in Au, as shown in Figs. S3(c and f), respectively. Small separation leads to large optical confinement leading to the generation of sufficient density of energetic hot electrons. Once accumulated on the surface of the nanosphere, the hot electrons transfer to the semiconductor following an indirect or a direct pathway. In an indirect process, the plasmonic hot electrons which acquire sufficient energy to move above the Fermi level migrate to the semiconductor surface (Fig. S10(a)). However, those plasmonic hot electrons near the Fermi surface involves in a direct excitation to the conduction band of the semiconductor (Fig. S10(b)) [59]. We speculate that it is achieved by semiconductor defect-plasmon interaction following a quantum tunneling process. The recent studies of Xue et al. [60], Tan et al. [61], and Naldoni et al. [62] have demonstrated the defect-mediated plasmonic excitation from metal to a semiconductor. Our XPS study has shown that Ti^{3+} content in Au–TiO_2 is 8.1% and in Ag–TiO_2 this concentration is 10.3%. The Ti^{3+} states have an energy distribution up to 0.8–1 eV below the conduction band edge of TiO_2 [63]. Therefore, the low energy hot electrons near the Fermi surface can migrate to the metal-semiconductor interface and undergo quantum tunneling to the defect states [64,65]. The plasmon-defect interaction activates defect electrons and triggers their excitation to the conduction band of TiO_2. One primary criterion for efficient quantum tunneling is to reduce the depletion layer width. Because of the lower position of Fermi level of Au and Ag than that of the conduction band edge position of TiO_2, the electrons will flow from semiconductor to metal. It leads to a negative charging on the metal surface and formation of a depletion barrier at the metal-semiconductor interface. The excess cationic Ti^{3+} on the TiO_2 surface can neutralize the accumulated negative charge on the plasmonic metal leading to a narrowing of the depletion width [65]. A narrowed depletion layer width increases the possibility of quantum tunneling of the plasmonic electrons from the near Fermi surface to the conduction band. Once the free electrons populate the surface of TiO_2, they form hydroxyl and superoxide radicals. These radicals interact with the surface adsorbed RhB/phenol leading to its degradation.

3.5.2. Ag–TiO_2–CN and Au–TiO_2–CN

Next, we discuss the mechanism of superior photocatalytic activity displayed by Ag–TiO_2–CN and Au–TiO_2–CN ternary hybrids. The pictorial representation of this process is shown in Fig. 12. Along with hot electron generation and injection, the interfacial charge transfer is an additive for the enhanced photocatalytic activity in the three component plasmonic photocatalyst. Those hot electrons acquiring sufficient energy to cross the Schottky barrier can pass on to the semiconductor. The rest of the low energetic electrons near the Fermi surface are excited to the conduction band of TiO_2 via the intermediate defect states. The electrons from CB of TiO_2 transfer to the CB of CN, which possesses an extended 2D network of C, N bondings, as depicted in Fig. 12. CN nanosheets absorb a portion of visible light below 470 nm. In the heterostructure Ag or Au is in contact with CN also. Thus, under visible light exposure, a strong plasmonic field accumulates at the interface of metal-TiO_2 and metal-CN as well, as shown in Fig. 12. The active optical field could facilitate electronic excitation from VB of CN to the nitrogenated defect states in CN, which finally got transferred to the CB of CN under visible light. Thus, once shifted to CN, the electrons could easily transport to a distant position over the 2D surface away from the interface, thus reducing the carrier recombination probability. The electrons residing on the surface of CN generate superoxide radicals, interact with RhB and phenol, and results in their decomposition.

Thus, the enhancement of photocatalysis in the binary system is due to the hot electron injection from Ag (or Au) to TiO_2. We believe that the increase in photocatalytic activity in the ternary composites is due to the hot electron injection either through quantum tunneling or via the intermediate states. This is assisted by the interfacial charge transfer

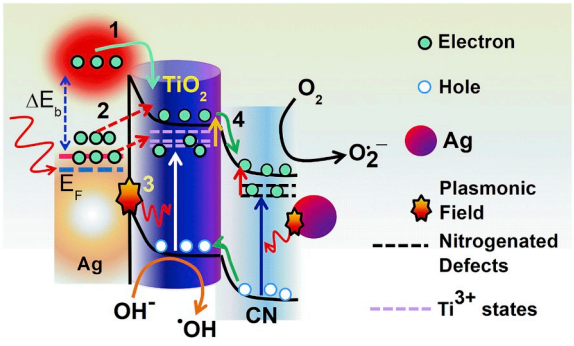

Fig. 12. Schematic illustration of photocatalysis in Ag-TiO2-CN: (1) Plasmonic hot electrons with energy above the Fermi level cross the Schottky barrier and migrate to the conduction band (CB) of TiO_2. (2) Direct excitation of the hot electrons near the Fermi surface (E_F) to the CB of TiO_2 by activating Ti^{3+} states. (3) Activation of Ti^{3+} or nitrogenated defect states via the plasmonic field at the Ag–TiO_2 or Ag–CN interface. (4) Electron and hole migration at the junction between TiO_2 and CN and formation of superoxide and hydroxyl radicals. These active radicals finally involve in RhB degradation.

from TiO_2 to CN. Photoresponse study in the absence of external bias provides direct evidence of the contribution of interfacial charge transfer and hot electron injection mediated photocatalysis in the ternary systems.

4. Conclusions

In summary, our results show that ternary plasmonic HS of Ag–TiO_2–CN and Au–TiO_2–CN are quite efficient photocatalysts as compared to the binary hybrids of Ag–TiO_2 and Au–TiO_2 in the effective removal of RhB and phenol from water under the illumination of visible light. Uniformly dispersed Ag (Au) NPs have small inter-particle separation of ~3.4 nm (~4.7 nm), as revealed by TEM analysis and thus may possess numerous plasmonic hot spots in the system. In binary hybrids, these plasmonic hot spots region activate direct hot electron injection from plasmonic metal to conduction band of TiO_2 or via the intermediate defect states present in TiO_2. In the ternary HS of Ag–TiO_2–CN and Au–TiO_2–CN, the hot electron injection and the interfacial charge transfer from TiO_2 to CN is evidenced by photoresponse study selectively excited with plasmonic wavelengths, as suppresses the carrier recombination and accelerate the rate of photodegradation of pollutants. The most efficient photocatalyst, Ag–TiO_2–CN shows more than 6-fold enhancements in the photodecomposition rate of RhB/phenol over pristine TiO_2 and more than 7-fold increase over pristine CN. The interfacial charge transfer and hot electron injection mediate the enhanced photocatalysis in the ternary heterostructures.

Acknowledgment

BC would like to thank Department of Science and Technology (DST), Govt. of India for providing DST INSPIRE faculty award (IFA15/MS-62) to pursue this work. PKG would like to acknowledge the financial support from MEITY (Grant No. 5(9)/2012-NANO(VOL-II)) for carrying out part of this work. The authors would like to thank central instruments facility (CIF) IIT Guwahati for providing various characterisation facilities.

Appendix A. Supplementary data

Supplementary data to this article can be found online at https://doi.org/10.1016/j.solmat.2019.110053.

References

[1] A. Fujishima, K. Honda, Electrochemical photolysis of water at a semiconductor electrode, Nature 238 (1972) 37–38.
[2] K. Nakata, A. Fujishima, TiO_2 photocatalysis: design and applications, J. Photochem. Photobiol., C 13 (2012) 169–189.
[3] S. Paul, P. Chetri, B. Choudhury, G. Ameen Ahmed, A. Choudhury, Enhanced visible light photocatalytic activity of Gadolinium doped nanocrystalline titania: an experimental and theoretical study, J. Colloid Interface Sci. 439 (2015) 54–61.
[4] R. Daghrir, P. Drogui, D. Robert, Modified TiO_2 for environmental photocatalytic applications: a review, Ind. Eng. Chem. Res. 52 (2013) 3581–3599.
[5] J. Wang, D.N. Tafen, J.P. Lewis, Z. Hong, A. Manivannan, M. Zhi, M. Li, N. Wu, Origin of photocatalytic activity of nitrogen-doped TiO_2 nanobelts, J. Am. Chem. Soc. 131 (2009) 12290–12297.
[6] K.K. Paul, R. Ghosh, P.K. Giri, Mechanism of strong visible light photocatalysis by Ag_2O-nanoparticle-decorated monoclinic TiO_2(B) porous nanorods, Nanotechnology 27 (2016) 315703.
[7] Z. Wei Seh, W. Li, J.J. Cha, G. Zheng, Y. Yang, M.T. McDowell, P.-C. Hsu, Y. Cui, Sulphur–TiO_2 yolk–shell nanoarchitecture with internal void space for long-cycle lithium–sulphur batteries, Nat. Commun. 4 (2013) 1331.
[8] K.K. Paul, N. Sreekanth, R.K. Biroju, T.N. Narayanan, P.K. Giri, Solar light driven photoelectrocatalytic hydrogen evolution and dye degradation by metal-free few-layer MoS_2 nanoflower/TiO_2(B) nanobelts heterostructure, Sol. Energy Mater. Sol. Cells 185 (2018) 364–374.
[9] N. Wu, Plasmonic metal–semiconductor photocatalysts and photoelectrochemical cells: a review, Nanoscale 10 (2018) 2679–2696.
[10] K.K. Paul, P.K. Giri, Role of surface plasmons and hot electrons on the multi-step photocatalytic decay by defect enriched Ag@TiO_2 nanorods under visible light, J. Phys. Chem. C 121 (2017) 20016–20030.
[11] R.K. Biroju, B. Choudhury, P.K. Giri, Plasmon-enhanced strong visible light photocatalysis by defect engineered CVD graphene and graphene oxide physically functionalized with Au nanoparticles, Catal. Sci. Technol. 6 (2016) 7101–7112.
[12] M. Kim, M. Lin, J. Son, H. Xu, J.-M. Nam, Hot-electron-mediated photochemical reactions: principles, recent advances, and challenges, Adv. Opt. Mater. 5 (2017) 1700004.
[13] T.G.U. Ghobadi, A. Ghobadi, E. Ozbay, F. Karadas, Strategies for plasmonic hot-electron-driven photoelectrochemical water splitting, ChemPhotoChem 2 (2017) 161–182.
[14] X. Wei, C. Shao, X. Li, N. Lu, K. Wang, Z. Zhang, Y. Liu, Facile in situ synthesis of plasmonic nanoparticles-decorated g-C_3N_4/TiO_2 heterojunction nanofibers and comparison study of their photosynergistic effects for efficient photocatalytic H2 evolution, Nanoscale 8 (2016) 11034–11043.
[15] Y. Chen, W. Huang, D. He, Y. Situ, H. Huang, Construction of heterostructured g-C_3N_4/Ag/TiO_2 microspheres with enhanced photocatalysis performance under visible-light irradiation, ACS Appl. Mater. Interfaces 6 (2014) 14405–14414.
[16] Y. Zou, J.-W. Shi, D. Ma, Z. Fan, C. Niu, L. Wang, Fabrication of g-C_3N_4/Au/C-TiO_2 hollow structures as visible-light-driven Z-scheme photocatalysts with enhanced photocatalytic H_2 evolution, ChemCatChem 9 (2017) 3752–3761.
[17] M. Zang, L. Shi, L. Liang, D. Li, J. Sun, Heterostructured g-C_3N_4/Ag–TiO_2 composites with efficient photocatalytic performance under visible-light irradiation, RSC Adv. 5 (2015) 56136–56144.
[18] J. Li, W. Wan, H. Zhou, J. Li, D. Xu, Hydrothermal synthesis of TiO_2(B) nanowires with ultrahigh surface area and their fast charging and discharging properties in Li-ion batteries, Chem. Commun. 47 (2011) 3439–3441.
[19] X. Yan, Y. Li, M. Li, Y. Jin, F. Du, G. Chen, Y. Wei, Ultrafast lithium storage in TiO_2–bronze nanowires/N-doped graphene nanocomposites, J. Mater. Chem. 3 (2015) 4180–4187.
[20] B. Choudhury, P.K. Giri, Isotype heterostructure of bulk and nanosheets of graphitic carbon nitride for efficient visible light photodegradation of methylene blue, RSC Adv. 6 (2016) 24976–24984.
[21] P.C. Lee, D. Meisel, Adsorption and surface-enhanced Raman of dyes on silver and gold sols, J. Phys. Chem. 86 (1982) 3391–3395.
[22] J. Kimling, M. Maier, B. Okenve, V. Kotaidis, H. Ballot, A. Plech, Turkevich method for gold nanoparticle synthesis revisited, J. Phys. Chem. B 110 (2006) 15700–15707.
[23] R. Gone, C. Biswajit, P.K. Giri, In situ decoration of plasmonic Au nanoparticles on graphene quantum dots-graphitic carbon nitride hybrid and evaluation of its visible light photocatalytic performance, Nanotechnology 28 (2017) 395703.
[24] W. Li, C. Ran, R. Zhi-Fei, G. Cai-Wang, L. Zhen-Xing, H. Shu-Juan, Y. Yong-Qiang, W. Chun-Yan, L. Lin-Bao, Plasmonic silver nanosphere enhanced ZnSe nanoribbon/Si heterojunction optoelectronic devices, Nanotechnology 27 (2016) 215202.
[25] T. Beuvier, M. Richard-Plouet, L. Brohan, Accurate methods for quantifying the relative ratio of anatase and TiO_2(B) nanoparticles, J. Phys. Chem. C 113 (2009) 13703–13706.
[26] Y. Zhang, Z. Xing, X. Liu, Z. Li, X. Wu, J. Jiang, M. Li, Q. Zhu, W. Zhou, Ti^{3+} self-doped blue TiO2(B) single-crystalline nanorods for efficient solar-driven photocatalytic performance, ACS Appl. Mater. Interfaces 8 (2016) 26851–26859.
[27] C.Y. Xu, P.X. Zhang, L. Yan, Blue shift of Raman peak from coated TiO_2 nanoparticles, J. Raman Spectrosc. 32 (2001) 862–865.
[28] X. Pan, M.-Q. Yang, Z.-R. Tang, Y.-J. Xu, Noncovalently functionalized graphene-directed synthesis of ultralarge graphene-based TiO_2 nanosheet composites: tunable morphology and photocatalytic applications, J. Phys. Chem. C 118 (2014) 27325–27335.
[29] A. Zielińska-Jurek, E. Kowalska, J.W. Sobczak, W. Lisowski, B. Ohtani, A. Zaleska, Preparation and characterization of monometallic (Au) and bimetallic (Ag/Au) modified-titania photocatalysts activated by visible light, Appl. Catal., B 101 (2011) 504–514.
[30] B. Santara, P.K. Giri, K. Imakita, M. Fujii, Evidence of oxygen vacancy induced room temperature ferromagnetism in solvothermally synthesized undoped TiO_2 nanoribbons, Nanoscale 5 (2013) 5476–5488.
[31] P. Krishnan, M. Liu, P.A. Itty, Z. Liu, V. Rheinheimer, M.-H. Zhang, P.J.M. Monteiro, L.E. Yu, Characterization of photocatalytic TiO_2 powder under varied environments using near ambient pressure X-ray photoelectron spectroscopy, Sci. Rep. 7 (2017) 43298.
[32] J. Zhang, A. Byeon, J.W. Lee, Boron-doped carbon–iron nanocomposites as efficient oxygen reduction electrocatalysts derived from carbon dioxide, Chem. Commun. 50 (2014) 6349–6352.
[33] M. Zhang, Z. Liu, Y. Gao, L. Shu, Ag modified g-C_3N_4 composite entrapped PES UF membrane with visible-light-driven photocatalytic antifouling performance, RSC Adv. 7 (2017) 42919–42928.
[34] N.S.R.D.N. NIST, X-ray Photoelectron Spectroscopy Database, National Institute of Standards and Technology, Gaithersburg MD, 2000, p. 20899, https://doi.org/10.18434/T4T88K retrieved on 14-12-2018.
[35] S.J. Tauster, Strong metal-support interactions, Acc. Chem. Res. 20 (1987) 389–394.
[36] H. Tang, Y. Su, B. Zhang, A.F. Lee, M.A. Isaacs, K. Wilson, L. Li, Y. Ren, J. Huang, M. Haruta, B. Qiao, X. Liu, C. Jin, D. Su, J. Wang, T. Zhang, Classical strong metal–support interactions between gold nanoparticles and titanium dioxide, Sci. Adv. 3 (2017) e1700231.
[37] Y. Horiguchi, T. Kanda, K. Torigoe, H. Sakai, M. Abe, Preparation of gold/silver/titania trilayered nanorods and their photocatalytic activities, Langmuir 30 (2014) 922–928.
[38] S. Melissen, T. Le Bahers, S.N. Steinmann, P. Sautet, Relationship between carbon nitride structure and exciton binding energies: a DFT perspective, J. Phys. Chem. C 119 (2015) 25188–25196.
[39] L. Xiang, X. Zhao, C. Shang, J. Yin, Au or Ag nanoparticle-decorated 3D urchin-like

TiO_2 nanostructures: synthesis, characterization, and enhanced photocatalytic activity, J. Colloid Interface Sci. 403 (2013) 22–28.
[40] P. Zhang, T. Wang, J. Gong, Mechanistic understanding of the plasmonic enhancement for solar water splitting, Adv. Mater. 27 (2015) 5328–5342.
[41] A. Stevanovic, S. Ma, J.T. Yates, Effect of gold nanoparticles on photoexcited charge carriers in powdered TiO_2 − long range quenching of photoluminescence, J. Phys. Chem. C 118 (2014) 21275–21280.
[42] B. Choudhury, K.K. Paul, D. Sanyal, A. Hazarika, P.K. Giri, Evolution of nitrogen-related defects in graphitic carbon nitride nanosheets probed by positron annihilation and photoluminescence spectroscopy, J. Phys. Chem. C 122 (2018) 9209–9219.
[43] K. Wu, Q. Li, Y. Du, Z. Chen, T. Lian, Ultrafast exciton quenching by energy and electron transfer in colloidal CdSe nanosheet–Pt heterostructures, Chem. Sci. 6 (2015) 1049–1054.
[44] M.D.L. Ruiz Peralta, U. Pal, R.S. Zeferino, Photoluminescence (PL) quenching and enhanced photocatalytic activity of Au-decorated ZnO nanorods fabricated through microwave-assisted chemical synthesis, ACS Appl. Mater. Interfaces 4 (2012) 4807–4816.
[45] B. Choudhury, A. Choudhury, Oxygen defect dependent variation of band gap, Urbach energy and luminescence property of anatase, anatase–rutile mixed phase and of rutile phases of TiO_2 nanoparticles, Physica E 56 (2014) 364–371.
[46] N.T. Khoa, S.W. Kim, D.-H. Yoo, S. Cho, E.J. Kim, S.H. Hahn, Fabrication of Au/graphene-wrapped ZnO-nanoparticle-assembled hollow spheres with effective photoinduced charge transfer for photocatalysis, ACS Appl. Mater. Interfaces 7 (2015) 3524–3531.
[47] C.G. Silva, M.J. Sampaio, S.A.C. Carabineiro, J.W.L. Oliveira, D.L. Baptista, R. Bacsa, B.F. Machado, P. Serp, J.L. Figueiredo, A.M.T. Silva, J.L. Faria, Developing highly active photocatalysts: gold-loaded ZnO for solar phenol oxidation, J. Catal. 316 (2014) 182–190.
[48] Q. Hu, W. Zheng, R. Lin, Y. Xu, F. Huang, Oxides/graphene heterostructure for deep-ultraviolet photovoltaic photodetector, Carbon 147 (2019) 427–433.
[49] C.-J. Chen, C.-H. Liao, K.-C. Hsu, Y.-T. Wu, J.C.S. Wu, P–N junction mechanism on improved NiO/TiO2 photocatalyst, Catal. Commun. 12 (2011) 1307–1310.
[50] L.J. Brennan, F. Purcell-Milton, A.S. Salmeron, H. Zhang, A.O. Govorov, A.V. Fedorov, Y.K. Gun'ko, Hot plasmonic electrons for generation of enhanced photocurrent in gold-TiO_2 nanocomposites, Nanoscale Res. Lett. 10 (2015) 38.
[51] N. Boonprakob, N. Wetchakun, S. Phanichphant, D. Waxler, P. Sherrell, A. Nattestad, J. Chen, B. Inceesungvorn, Enhanced visible-light photocatalytic activity of g-C_3N_4/TiO_2 films, J. Colloid Interface Sci. 417 (2014) 402–409.
[52] Z. Jiang, D. Liu, D. Jiang, W. Wei, K. Qian, M. Chen, J. Xie, Bamboo leaf-assisted formation of carbon/nitrogen co-doped anatase TiO_2 modified with silver and graphitic carbon nitride: novel and green synthesis and cooperative photocatalytic activity, Dalton Trans. 43 (2014) 13792–13802.
[53] Z. Zhao, J. Tian, D. Wang, X. Kang, Y. Sang, H. Liu, J. Wang, S. Chen, R.I. Boughton, H. Jiang, UV-visible-light-activated photocatalysts based on Bi_2O_3/$Bi_4Ti_3O_{12}$/TiO_2 double-heterostructured TiO_2 nanobelts, J. Mater. Chem. 22 (2012) 23395–23403.
[54] Z. Xiong, L.L. Zhang, J. Ma, X.S. Zhao, Photocatalytic degradation of dyes over graphene–gold nanocomposites under visible light irradiation, Chem. Commun. 46 (2010) 6099–6101.
[55] L.-L. Tan, W.-J. Ong, S.-P. Chai, A.R. Mohamed, Noble metal modified reduced graphene oxide/TiO_2 ternary nanostructures for efficient visible-light-driven photoreduction of carbon dioxide into methane, Appl. Catal., B 166–167 (2015) 251–259.
[56] L.V. Besteiro, A.O. Govorov, Amplified generation of hot Electrons and quantum surface effects in nanoparticle dimers with plasmonic hot spots, J. Phys. Chem. C 120 (2016) 19329–19339.
[57] X.-T. Kong, Z. Wang, A.O. Govorov, Plasmonic nanostars with hot spots for efficient generation of hot electrons under solar illumination, Adv. Opt. Mater. 5 (2016).
[58] T.-H. Yang, Y.-W. Harn, M.-Y. Pan, L.-D. Huang, M.-C. Chen, B.-Y. Li, P.-H. Liu, P.-Y. Chen, C.-C. Lin, P.-K. Wei, L.-J. Chen, J.-M. Wu, Ultrahigh density plasmonic hot spots with ultrahigh electromagnetic field for improved photocatalytic activities, Appl. Catal., B 181 (2016) 612–624.
[59] S.K. Cushing, Plasmonic hot carriers skip out in femtoseconds, Nat. Photonics 11 (2017) 748–749.
[60] J. Xue, O. Elbanna, S. Kim, M. Fujitsuka, T. Majima, Defect state-induced efficient hot electron transfer in Au nanoparticles/reduced TiO_2 mesocrystal photocatalysts, Chem. Commun. 54 (2018) 6052–6055.
[61] S. Tan, A. Argondizzo, J. Ren, L. Liu, J. Zhao, H. Petek, Plasmonic coupling at a metal/semiconductor interface, Nat. Photonics 11 (2017) 806–812.
[62] A. Naldoni, F. Fabbri, M. Altomare, M. Marelli, R. Psaro, E. Selli, G. Salviati, V. Dal Santo, The critical role of intragap states in the energy transfer from gold nanoparticles to TiO_2, Phys. Chem. Chem. Phys. 17 (2015) 4864–4869.
[63] A. Naldoni, M. Allieta, S. Santangelo, M. Marelli, F. Fabbri, S. Cappelli, C.L. Bianchi, R. Psaro, V. Dal Santo, Effect of nature and location of defects on bandgap narrowing in black TiO_2 nanoparticles, J. Am. Chem. Soc. 134 (2012) 7600–7603.
[64] A.M. Elsharif, The effect of the electron tunneling on the photoelectric hot electrons generation in metallic-semiconductor nanostructures, Chem. Phys. Lett. 691 (2018) 224–230.
[65] Y. Shiraishi, N. Yasumoto, J. Imai, H. Sakamoto, S. Tanaka, S. Ichikawa, B. Ohtani, T. Hirai, Quantum tunneling injection of hot electrons in Au/TiO_2 plasmonic photocatalysts, Nanoscale 9 (2017) 8349–8361.